Computational Materials Science 184 (2020) 109938

Contents lists available at ScienceDirect

Computational Materials Science

journal homepage: www.elsevier.com/locate/commatsci

Thermal conductivity of monolayer hexagonal boron nitride: From defective to amorphous

Xin Wu, Qiang Han*

Department of Engineering Mechanics, School of Civil Engineering and Transportation, South China University of Technology, Guangzhou, Guangdong Province 510640, People's Republic of China

ARTICLE INFO

Keywords:
Thermal conductivity
Defective h-BN
Two-dimentional amorphous BN
Molecular dynamics
Graphics processing units

ABSTRACT

Through extensive molecular dynamics simulations, we completed the thermal transport properties study of the monolayer hexagonal boron nitride (h-BN) films from the defect state to the amorphous state. To this end, a defective h-BN model construction program has been developed, which can customize the nature of the defects and realize the transition from the defect state to the amorphous state. By performing homogeneous non-equilibrium molecular dynamics simulations based on Tersoff multi-body potential, the thermal conductivity results of large-size h-BN films have been achieved. For the defect state h-BN, we studied the effect of different defect types and concentrations on its thermal conductivity and verified it from the phonon mechanism. After the transition to two-dimensional amorphous BN, we discussed and analyzed the influence of amorphous concentration, amorphous defect ratio and temperature on its thermal transport properties. On this basis, the restriction relationship between phonon-phonon scattering term and phonon-defect scattering term was also proposed from the atomic level mechanisms. Our results constitute a step in the deterministic engineering of thermal management devices in 2D materials, and hold great promise for the application of h-BN defect engineering in the field of nanomaterial thermal design.

1. Introduction

In recent years, a class of two-dimensional (2D) materials represented by graphene has been widely hailed by academics for its monoatomic thickness and some exceptional physical and chemical properties that are different from other materials [1,2]. Owing to the strong in-plane covalent bonds similar to graphene, hexagonal boron nitride (h-BN) known as "white graphene" has outstanding optical properties [3,4], strong mechanical properties [5,6], ultra-high thermal conductivity [7–10] and excellent chemical stability [11,12]. However, unlike the electrical conductivity of graphene, h-BN is endowed special electrical insulation, which makes it a candidate for thermal management directly below a new generation of electronic products [13,14]. The above factors stimulate intensive research efforts on the pivotal issue, thermal conductivity, in thermal applications of h-BN, both experimentally and theoretically.

According to reports, the basal-plane thermal conductivity measurement of bulk h-BN based on pulse heating technique can reach 390 $Wm^{-1} K^{-1}$ [7]. However, the thermal conductivity obtained by recent experiments are about 360 $Wm^{-1} K^{-1}$in suspended multilayer (11–12 atomic thickness) h-BN by micro-bridge device with built-in thermometers [8] and around 484 $Wm^{-1} K^{-1}$ (+141 $Wm^{-1} K^{-1}$/−24 $Wm^{-1} K^{-1}$) in bilayer h-BN measured by pre-patterned microstructure [9], respectively. Due to the interlayer interaction, the out-of-plane acoustic phonons of the multilayer h-BN will be more strongly suppressed and therefore exhibit lower thermal conductivity. Hao et al. [10] measured the thermal conductivity of monolayer single-crystalline h-BN using the opto-thermal Raman technique to be 544.6 ± 77.5 $Wm^{-1} K^{-1}$, which have good consistency with the result of more than 600 $Wm^{-1} K^{-1}$ obtained by the accurate numerical solution of the phonon Boltzmann transport equation [15]. The existing 2D material preparation technology mainly includes mechanical peeling method, chemical vapor deposition(CVD) and pyrolysis method, just to name a few here [16–18]. The prepared samples will inevitably contain some structural defects, such as vacancies, dislocations and grain boundaries, and even the amorphous [18–20]. Under such circumstances, the defect engineering used for material performance control also came into being. Insofar, clearly understanding the influence of various structural defects on the thermal transport properties of h-BN is an indispensable work in the field of thermal management of 2D materials.

Admittedly, due to the limitations of experimental preparation and

* Corresponding author.
E-mail address: emqhan@scut.edu.cn (Q. Han).

https://doi.org/10.1016/j.commatsci.2020.109938
Received 14 May 2020; Received in revised form 2 July 2020; Accepted 12 July 2020

characterization, molecular dynamics (MD) simulation becomes a commonly used and effective method to study the properties of materials. In the field of thermal conductivity calculation of nanomaterials, the commonly used MD methods are mainly non-equilibrium molecular dynamics (NEMD) method based on Fourier law and equilibrium molecular dynamics (EMD) method in view of Green–Kubo equation [21,22]. These simulation studies are often by means of open-source software large-scale atomic/molecular massively parallel simulator (LAMMPS) [23]. Using the NEMD method, Chen et al. [24] and Zhu et al. [25] got the results of $265 \pm 120\ \mathrm{Wm^{-1}\,K^{-1}}$ and $650 \pm 25\ \mathrm{Wm^{-1}\,K^{-1}}$ for the thermal conductivity of monolayer h-BN, respectively. For the EMD method that is less affected by the size effect, the simulation results obtained by Mahdi Zadeh et al. [26] and Khan et al. [27] are $550 \pm 60\ \mathrm{Wm^{-1}\,K^{-1}}$ and around $649\ \mathrm{Wm^{-1}\,K^{-1}}$, respectively. The research work by Mortazavi et al. [28,29] showed that the thermal conductivity result of monolayer h-BN is about $80\ \mathrm{Wm^{-1}\,K^{-1}}$ obtained by NEMD method and based on EMD method. Recent studies [30,31] have shown that the calculation of the instantaneous heat flux in LAMMPS is incorrect for multi-body potentials, which leads to an underestimation of the thermal conductivity of the such materials, including h-BN.

In this paper, the thermal conductivity of monolayer h-BN is studied based on extensive large-scale MD simulations. Firstly, the thermal conductivity of pristine monolayer h-BN was calculated by the efficient homogeneous non-equilibrium molecular dynamics (HNEMD) method [32–36], and the cross-checking was also performed with the EMD method. Next, the HNEMD method was used to study the thermal transport properties of h-BN with three different structural defects, which includes monovacancy, divacancy, and Stone–Wales (SW) defects. Then from the perspective of phonon, the effects and specific causes of the above three defects on h-BN heat transport properties were analyzed. Finally, the h-BN transited from the defect state to the amorphous state. We explored the specific effects of the amorphous concentration, the amorphous defect ratio, and temperature on its thermal conductivity, and conducted a qualitative analysis from the phonon perspective. The restriction relationship between the phonon–phonon scattering term and the phonon-defect scattering term in controlling the thermal conductivity of two-dimensional amorphous BN (2D-aBN) was also proposed.

2. Model and method

An algorithm specially designed for modeling has been developed, which can realize the construction of monolayer defective h-BN and 2D-aBN models with randomly distributed defects, specified defect types and concentrations. The MD simulations in this work were all implemented by the efficient graphics processing units molecular dynamics (GPUMD) code [37–39], which applies an accurate heat flux formula suitable for multi-body potentials and avoids errors in LAMMPS. The Tersoff empirical potential optimized by Sevik et al. [40] was used, which re-parameterizes the original empirical potential to further accurately represent the experimental structure and phonon dispersion law of the 2D h-BN.

2.1. Models for 2D defective and amorphous BN

In this study, we chose a square h-BN with an in-plane dimension of 40 nm × 40 nm in which the total number of atoms is 59892. On this basis, three common structural defects in graphene-like materials [41–43], monovacancy, divacancy and SW defects were introduced to build the defect h-BN atomic structure, as shown in Fig. 1(c–e) for an illustration. Due to the difference of nitrogen and boron atoms in the h-BN, monovacancy defects have two different orientations according to the type of missing atoms. In addition, we characterized divacancy and SW defects with the absence and in-plane 90° rotation of nitrogen-boron bonds and bonding atoms, respectively. In the hexagonal rings structure of 2D h-BN, the nitrogen-boron bonds have three different orientations, which also determines the three different orientations of these two defects. In the process of defects introduction, the randomness of its distribution includes two aspects: position randomness and orientation randomness. Undisputed, this is a sound way to avoid the particularity of the sample with defects. Apart from the above, the defects concentration is defined as the ratio of the number of non–hexagonal rings in the defective or 2D-aBN sample with respect to the total number of hexagonal rings in the initial pristine sample.

At a relatively higher defects concentration, two different types of defects, divacancy and SW, were introduced into pristine h-BN according to a certain proportional relationship to achieve the construction of 2D-aBN, as illustrated in Fig. 1(a-b). This is similar to the structure of 2D amorphous carbon [44–46], in which a large number of hexagonal rings are replaced by non–hexagonal rings such as pentagon rings and heptagon rings. In recent studies, Wegner et al. [18] prepared 2D-aBN by pyrolysis of hydrogen-rich (NH4)3Mg(BH4)5, which also provides the basis for the amorphous structure in this work.

2.2. MD methods for thermal conductivity calculation

2.2.1. The HNEMD method

The HNEMD method, first proposed by Evans [32], calculates the transport coefficient by defining the thermal transport process as a mechanical analog. In the past 40 years, this method has completed the development from two-body potential by Evans to cluster potential (a special kind of multi-body potential) by Mandadapu et al. [33] to all multi-body potentials by Fan et al. [34]. Under the desired temperature conditions, this method mimics the effect of thermal gradient by applying a suitable fictitious force field with a fixed direction to the system, and realizes the calculation of thermal conductivity by the linear response of the virial heat flux vector with respect to the fictitious force field. Note that in the following formula, the kinetic term will be generally ignore which does not contribute to the solid thermal conductivity [47].

The homogeneous heat current in this method is achieved by applying the following external driving force $\vec{F}_i^e$ to the particles i:

$$\vec{F}_i^e = \sum_{j \neq i} \left(\frac{\partial U_j}{\partial \vec{r}_{ji}} \otimes \vec{r}_{ij} \right) \cdot \vec{F}_e \tag{1}$$

where $U_j$is the site potential associated with the particle j. $\vec{r}_{ji}$and $\vec{r}_{ij}$are the position vector between particle $i$and j. $\vec{F}_i^e$ is the vector parameter for controlling the direction and magnitude of external driving force.

In a multi-body system, the interatomic interaction added to particle $i$can be expressed as:

$$\vec{F}_i^i \equiv -\frac{\partial U}{\partial \vec{r}_i} = \sum_{j \neq i} \left(\frac{\partial U_i}{\partial \vec{r}_{ij}} - \frac{\partial U_j}{\partial \vec{r}_{ji}} \right) \tag{2}$$

These two parts constitute the total force of the particle i. In this process, in order to avoid the external driving force heating the system, a constant temperature needs to be achieved by a thermostat. At the same time, the average force of the entire system must be subtracted from the force received by each particle to achieve the purpose of conservation of the total momentum of the system, just as mentioned in Ref.[34,35]. For a monolayer h-BN described by a multi-body potential, the potential energy term of the heat flux vector can be expressed as:

$$\vec{J} = \sum_i \sum_{j \neq i} \vec{r}_{ij} \left(\frac{\partial U_j}{\partial \vec{r}_{ji}} \cdot \vec{v}_i \right) \tag{3}$$

The thermal conductivity at a given time $t$can be given by the following formula:

$$\kappa(t) = \frac{\langle \vec{J}(t) \rangle_{ne}}{TV\,|\vec{F}_e|} \tag{4}$$

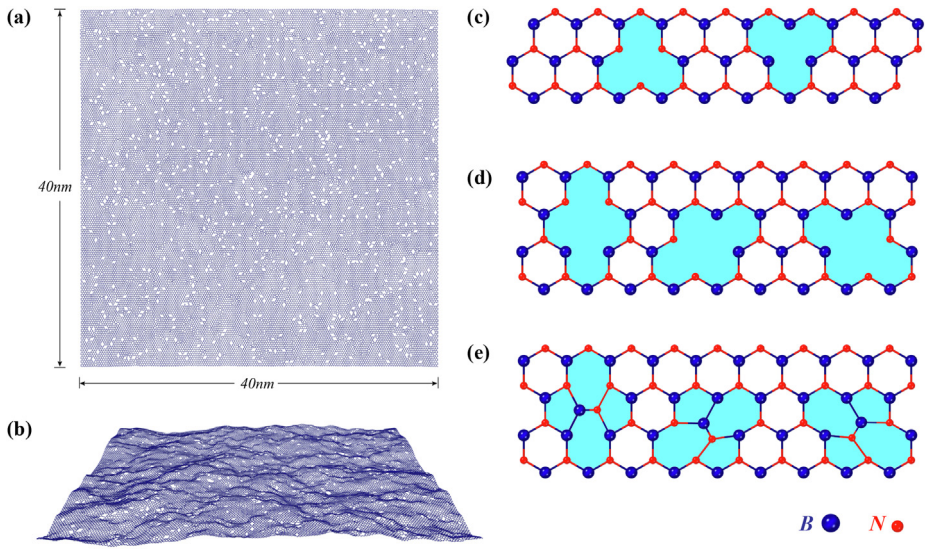

Fig. 1. Schematic illustration of the atomic structure of 2D-aBN and the structural defects in defective h-BN. (a) Top view of 2D-aBN with an in-plane size of 40 nm × 40 nm and defects concentration of 20%, in which the total number of atoms is 58412; (b) Side view of the above structure which has been fully relaxed with Tersoff potential [40] at 300 K; (c) Schematic diagram of monovacancy defects containing two different orientations; (d) Schematic diagram of divacancy defects containing three different orientations; (e) Schematic diagram of SW defects containing three different orientations. (The defect diagram is only used to describe how these defects formed. After thermal equilibrium, due to factors such as structural fluctuations, other complex defect structures may emerge, such as octagons.).

where $\langle\langle_{ne}$ is the average of non-equilibrium ensemble, which can be expressed as time average in MD simulation. *T*and *V* are the temperature of the simulation and the volume of the system, respectively. For the monolayer h-BN, the volume is generally considered to be the product of surface area and thickness of 0.335 nm. Further, in order to facilitate the observation of the convergence of $\kappa(t)$, it will be rewritten as the following form of cumulative average:

$$\kappa(t) = \frac{1}{t}\int_0^t \kappa(s)ds \tag{5}$$

In this calculation process, appropriate external force parameter $|\vec{F_e}|$ should be selected to ensure that a sufficiently large signal-to-noise ratio is obtained and the system could achieve a fully linear response. This needs to satisfy the condition $|\vec{F_e}|\ \lambda < 1/10$ [33], where $\lambda$is the mean free path. For the monolayer h-BN system, whether it is defective or not, $|\vec{F_e}| = 0.1\mu m^{-1}$ can meet the above requirements [36]. The periodic boundary conditions were applied in the in-plane direction of samples, and the out-of-plane direction remains free, so that the limited size effect can be ignored. For each set of independent simulations, the heat balance phase was carried out for 10 ns under the constant temperature and zero pressure conditions of the NPT ensemble, and then a homogeneous heat current was generated during the long output phase with for the calculation of thermal conductivity. We chose the time step of 1*fs*and repeated the average twice for each group of independent simulations, which is enough to reduce the error.

2.2.2. The EMD method

The EMD method, a method for calculating the thermal conductivity of materials based on the Green–Kubo [48,49] formula, relates the transport coefficient in the non-equilibrium state to the fluctuation of the corresponding physical quantity in the equilibrium state. The thermal conductivity tensor $\kappa_{\alpha\beta}(t)(\alpha, \beta = x, y, z)$ of a material can be expressed as:

$$\kappa_{\alpha\beta}(t) = \frac{1}{k_B T^2 V}\int_0^t \langle J_\alpha(0)J_\beta(t')\rangle dt' \tag{6}$$

where k_B is the Boltzmann constant, and the physical meaning of *T*and *V* is as described in the HNEMD method. The angle brackets in the heat current autocorrelation function (HCACF) $\langle J_\alpha(0)J_\beta(t')\langle_e$ represent the average at different time points, where *J*is as defined in Eq. (3).

In order to ignore the size effect as much as possible, the same boundary conditions as in the HNEMD method were adopted. For each set of independent simulations, the Berendsen thermostat was used at a given temperature to relax the system for 1 ns under the NVT ensemble. Then switch to the NVE ensemble for up to 10 ns of heat current data sampling. In the EMD method, the signal-to-noise ratio of HCACF will decrease as the correlation time increases. Therefore, each set of independent simulations needs to be repeated multiple times to obtain a more stable integrated thermal conductivity value. In the case of the time step of 1*fs*, each group of independent simulations was repeated for 16 times, and finally the average result was used as the thermal conductivity convergence value.

3. Results and discussion

3.1. Method validation with pristine h-BN

First, the HNEMD method was used to calculate the thermal conductivity of square pristine h-BN samples with five side lengths of 10 nm, 20 nm, 30 nm, 40 nm and 50 nm along two directions (armchair and zigzag direction). As shown in Table 1, for each group of samples, the results of the in-plane thermal conductivity in the two directions are slightly different. Unlike the monolayer black phosphorus, the thermal conductivity differs greatly in the two directions of armchair and zigzag [35]. In addition, the focus of this work is not on the anisotropy of thermal conductivity of h-BN. Therefore, the average value of the in-plane thermal conductivity in two directions was taken as the calculation result of the corresponding sample, which is also reasonable for

Table 1
Size effect and direction effect in the calculation of pristine h-BN thermal conductivity in $Wm^{-1}\ K^{-1}$ (The errors were calculated from the standard deviation of two independent simulation results).

Sample size	Number of atoms	$\kappa_{armchair}$	κ_{zigzag}	$\kappa_{average}$
10 nm × 10 nm	3936	690 ± 20	689 ± 21	689 ± 11
20 nm × 20 nm	15228	722 ± 10	650 ± 11	686 ± 4
30 nm × 30 nm	33880	647 ± 6	604 ± 19	625 ± 12
40 nm × 40 nm	59892	642 ± 4	669 ± 8	656 ± 4
50 nm × 50 nm	93264	657 ± 3	632 ± 12	644 ± 6

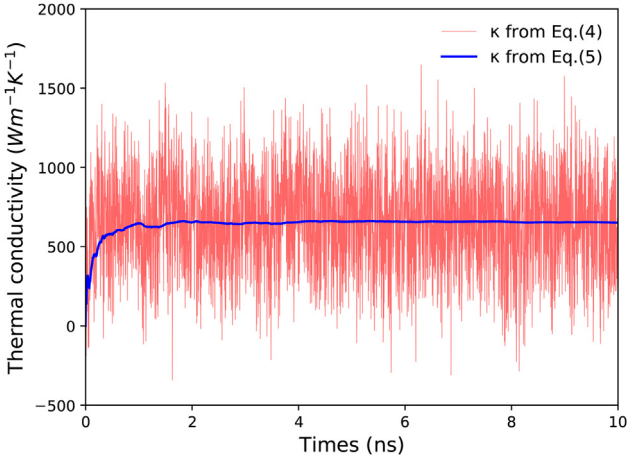

Fig. 2. Under the HNEMD method with a driving force parameter of $|\vec{F_e}| = 0.1\mu m^{-1}$, the calculation result of the in-plane thermal conductivity of monolayer h-BN with a size of 40 nm × 40 nm: The solid red line represents the result calculated by Eq. (4), and the solid blue line is the cumulative average result obtained by Eq. (5).

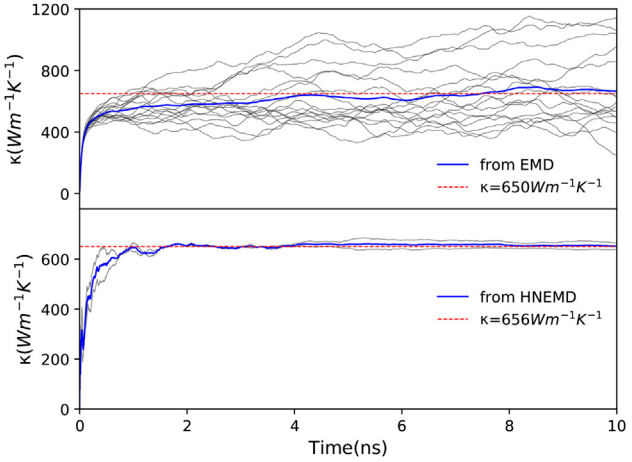

Fig. 3. Based on the EMD (the upper part) and HNEMD (the lower part) methods, the relationship between the thermal conductivity of the pristine h-BN with the size of 40 nm × 40 nm and the simulation time. (The solid black line represents the results of independent simulations, in which the EMD and HNEMD methods were performed 16 times and 2 times, respectively; The respective statistical average results are drawn in solid blue lines; The red dotted lines are the respective convergence reference lines, and their values are κ_{EMD} = 650 $Wm^{-1}K^{-1}$, κ_{HNEMD} = 656 $Wm^{-1}K^{-1}$, respectively).

2D materials. Note that all the in-plane thermal conductivity results of the monolayer h-BN described later are the average processing results in the in-plane two directions.

Next, a longitudinal comparative analysis of the results in Table 1 is performed. As the size of the simulated sample increases, the calculated thermal conductivity value decreases significantly and gradually stabilizes. This is due to the more violent out-of-plane deformation of the larger size samples, which will increase the phonon scattering caused by the acoustic bending mode, thereby significantly reducing the thermal conductivity. Simultaneously, sample with larger size will allow more long-wavelength phonons, which could increase the thermal conductivity. As the size of the sample increases further, the effects of the above two aspects compensate each other, resulting in the thermal conductivity gradually converging and tending to stabilize.

In order to take both the accuracy and cost of the simulation into account, a monolayer h-BN with a sufficiently large size of 40 nm × 40 nm was selected for the following study. The in-plane thermal conductivity results calculated by the HNEMD method are shown in Fig. 2. It is not difficult to find that the thermal conductivity result directly calculated by Eq. (4) fluctuates greatly with time, and the convergence of the result is not intuitive enough. However, the cumulative integration processing of the results in time can well reflect its good convergence, as described in Eq. (5).

The EMD method was used to calculate the in-plane thermal conductivity of the same h-BN sample in the calculation in Fig. 2 to crosscheck it, as plotted in Fig. 3. The result shows that the in-plane thermal conductivity is 650 ± 27 $Wm^{-1}K^{-1}$with 16 identical independent simulations by EMD method and 656 ± 4 $Wm^{-1}K^{-1}$with only 2 identical independent simulations by HNEMD method. The difference between the two results is negligible, but the former takes eight times as much output time as the latter. With the same calculation precision, HNEMD obviously needs less calculation cost. For an individual calculation, the HNEMD result of thermal conductivity tends to be stable and well-converged. In contrast, the results of EMD method exhibit large variations among each independent simulation, which means that multiple simulations need to be repeated to obtain the converged result. Therefore, the HNEMD method is clearly the better choice for current work.

As shown in Fig. 4, the above calculation results can be basically consistent with the existing research results, including experimental measured values [10], theoretical calculation results [15,25] and simulations based on different methods [24–29]. The 2-layer and bulk h-BN samples show lower thermal conductivity than the monolayer

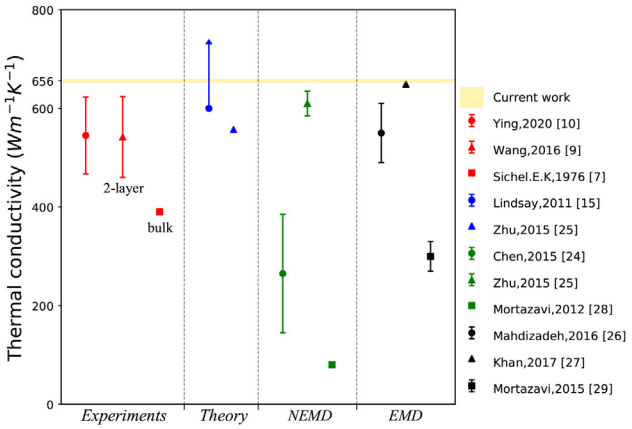

Fig. 4. Research results of in-plane thermal conductivity of monolayer pristine h-BN, double-layer and bulk h-BN at around 300 K; These include experimental measurements of thermal conductivity of monolayer, 2-layer and bulk h-BN (marked with text), theoretical calculation results of monolayer h-BN and MD simulations results based on NEMD and EMD methods of monolayer h-BN, respectively.

pristine samples due to the suppression of out-of-plane phonons by the interlayer van der Waals force. The thermal conductivity of the monolayer single-crystalline h-BN in Ref.[10] was measured at 315 K, which is slightly higher than our simulation temperature of 300 K. The temperature may be a factor causing the result to be slightly less than our calculation, which will be also discussed later. In addition, there are many uncertain factors in the experiments, including the temperature calibration error of the Raman spectrum peak position and so on. However, some MD simulations were constrained by factors such as the selection of potential function, the effect of sample size, and the inaccuracy of LAMMPS on the description of the multi-body potential heat flux formula, which led to these results much lower than the predicted values of this study.

3.2. Thermal conductivity of defective h-BN

Then we introduced three types of defects, monovacancy,

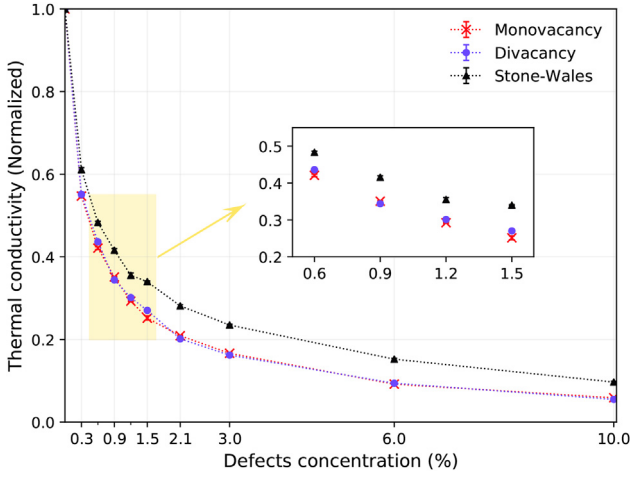

Fig. 5. The relationship between the normalized thermal conductivity and the defects concentration of the three types of defective h-BN (monovacancy, divacancy and SW defects) of the size of 40 nm × 40 nm at 300 K; It includes nine defects concentrations of 0.3%, 0.6%, 0.9%, 1.2%, 1.5%, 2.1%, 3%, 6% and 10%. (The detail diagram shows the specific datas of the yellow shaded part).

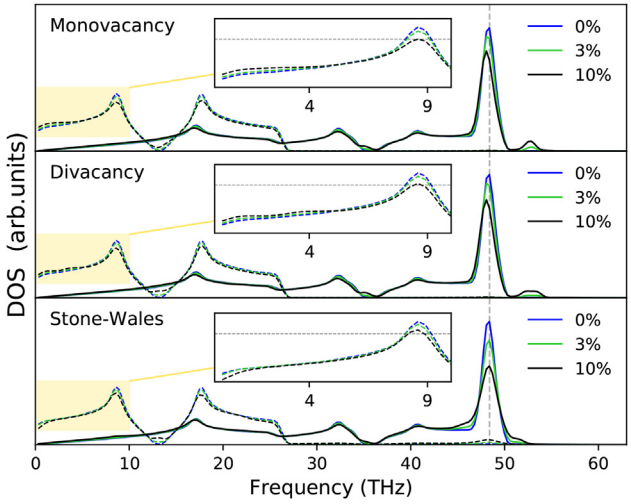

Fig. 6. Calculated DOS results of the pristine h-BN and three kinds of defective h-BN with defects concentration of 3% and 10%. The solid line indicates the in-plane part of DOS, and the dotted line indicates the out-of-plane part; The data in the 0-10THz frequency band (yellow shaded parts) are displayed in detail as a detailed diagram, in which three horizontal dashed lines are reference lines at the same amplitude. The vertical dashed line is the reference line at the frequency of 48THz, which is also the peak position of the in-plane DOS.

divacancy, and SW defects, on the monolayer pristine square h-BN sample of the size in 40 nm × 40 nm, as shown in Fig. 1. Each defective h-BN has the following nine defects concentration conditions: 0.3%, 0.6%, 0.9%, 1.2%, 1.5%, 2.1%, 3%, 6% and 10%. Since the focus of our work is the effect of defect type and concentration on the thermal conductivity of h-BN, we constructed three different samples by randomly setting defects for each concentration. And for each sample, two independent simulations with different initial speed seeds were performed. In the end, the statistical average result was used as the in-plane thermal conductivity result of a certain defective h-BN at a certain concentration, which can make the result persuasive.

As shown in Fig. 5, the normalized thermal conductivity calculation results of the three types of defective h-BN at 300 K in the above nine different concentrations. Obviously, the existence of defects has a strong weakening effect on the thermal conductivity of monolayer h-BN, which is caused by the phonon-defect scattering in the structure by the defects. Horizontal analysis of the data shows that as the defects concentration increases, the thermal conductivity of the three types of defective h-BN decreases significantly. At the same time, the rate of reduction in thermal conductivity tends to slow down with the increase of defects concentration. Specifically, when the defects concentration reaches 0.6%, its thermal conductivity value is lower than half of the pristine h-BN, which shows a cliff-like decline. When the defects concentration is increased to more than 3%, the decrease rate of the defective h-BN thermal conductivity is greatly slowed down. This means that even with a few defects, thermal conductivity of h-BN is still excellent compared to the dielectric substrates commonly used today, such as silicon dioxide. However, for h-BN with higher defects concentration, under the condition that the thermal conductivity satisfies the function, the concentration condition can become flexible to meet the specific needs of other properties, which is of great significance to the defect engineering of h-BN.

Next, a vertical comparison is carried out to analyze the difference in thermal conductivity results of different types of defects h-BN. It can be clearly observed that the difference between the two defects of monovacancy and divacancy on the thermal conductivity of h-BN is very slight, and even from the detail diagram in Fig. 5, these two parts of the data are almost identical. However, at the same concentration, the thermal conductivity of the defective h-BN with SW defects is significantly higher than that of the other two, which may be related to the defect formation style.

In order to further understand the basic influence mechanism of defects on the thermal conductivity of h-BN, three kinds of defective h-BN with the defects concentration of 3% and 10% were selected as samples for the phonon research. In Fig. 6, the phonon density of state (DOS) of the above samples at 300 K is plotted, which were obtained by performing the following Fourier integral transformation on the velocity autocorrelation function:

$$DOS_\alpha(\omega) = \int_{-\infty}^{+\infty} \langle v_\alpha(t) v_\alpha(0) \langle e^{-2\pi i \omega t} dt \ (\alpha = x, y, z) \tag{7}$$

where $\omega$is the frequency, $\langle v(t)v(0)\langle$ is the autocorrelation function of the velocity of the h-BN atoms at the correlation time t, αdetermines the vibration direction of the calculated phonon. When $\alpha = x$, it corresponds to the in-plane transverse acoustic mode(TA); When $\alpha = y$, it corresponds to the in-plane longitudinal acoustic mode(LA); When $\alpha = z$, it corresponds to the out-of-plane acoustic mode(ZA) of h-BN. In current work, the average value of TA and LA is taken as the overall in-plane acoustic model, and only in-plane and out-of-plane phonons are distinguished.

It is not difficult to find from the results in Fig. 6 that the introduction of defects has a significant effect on the phonon state density of h-BN. The in-plane DOS of the pristine h-BN (the solid blue line in the Fig. 6) peaks around 48THz. The out-of-plane DOS also shows two distinct peaks in the low frequency band less than 20THz, which accounts for the main contribution in thermal conductivity [50]. After the defects were introduced, the peak of the high-frequency DOS around 48THz is significantly attenuated; the peak in the low frequency band is reduced and the bandwidth is widened. And the greater the defects concentration, the more obvious the attenuation effect. These changes are the reflection of the scattering effect of defects on phonons, which makes the life of phonons shorter and results in a significant reduction in thermal conductivity. Next, the effect of different types of defects on the calculation of DOS at the same concentration is compared and discussed. Overall, the difference between the calculated DOS of monovacancy and divacancy h-BN is very tiny, which provides a strong proof for the similar results of the thermal conductivity of the two. For the defective h-BN with SW defects, the attenuation effect of the phonon state density in the high frequency band seems to be more serious. However, at low frequency bands less than 4THz and low frequency peaks near 9THz, h-BN is obviously more resistant to the DOS attenuation effect caused by SW defects, which is the main contributor

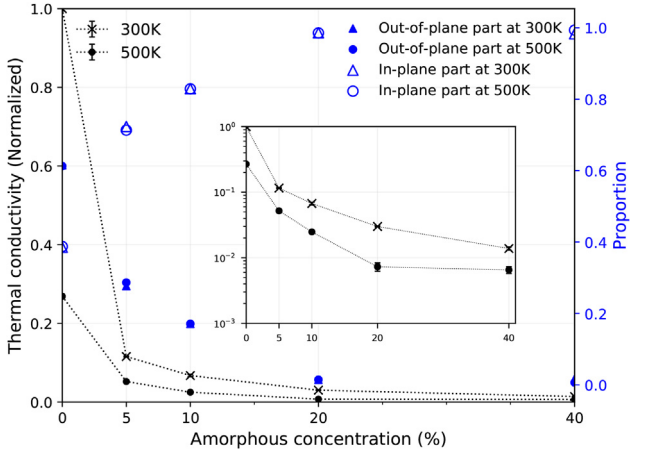

Fig. 7. At 300 K and 500 K, normalized thermal conductivity and the proportion of its in-plane and out-of-plane components of 2D-aBN with the amorphous defect ratio of 1:1 as a function of amorphous concentration. When the amorphous concentration is less than 10%, h-BN is the pristine and defect state; When it is above 10%, the sample belongs to the category of 2D-aBN. In order to more clearly reflect the data results, the normalized thermal conductivity based on the logarithmic coordinates is plotted in the detail diagram.

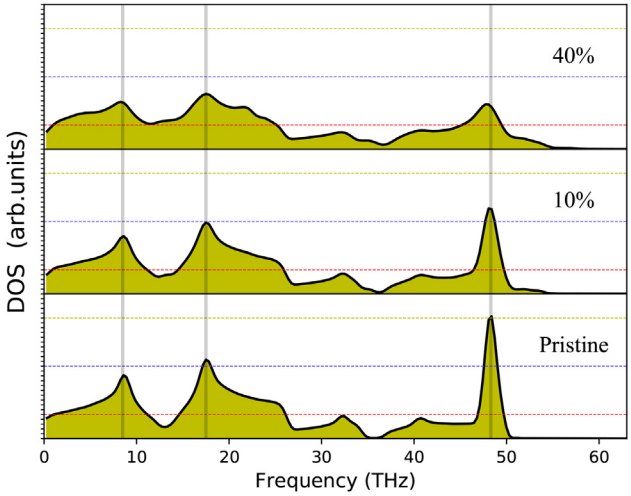

Fig. 8. At 300 K, the calculated DOS of the pristine h-BN and the 2D-aBN with amorphous concentration of 10% and 40% in Fig. 7. For easy comparison, the horizontal reference lines with the same calculated DOS value in the three subpictures are marked in the same color and the three vertical reference lines correspond to the peak positions. The position of the six reference lines crossing each other can be used as a comparison benchmark, which can clearly observe the change of DOS at the peak position.

in thermal conductivity. This also means that at the same concentration, the thermal conductivity of the defective h-BN with SW defects is significantly higher than the other two, which explains the calculation results in Fig. 5 well.

3.3. Thermal conductivity of 2D-aBN

As described in 2.1, since the monovacancy and divacancy defects have similar effects on the thermal conductivity of h-BN, relatively more divacancy and SW defects were simultaneously introduced into the pristine h-BN to construct 2D-aBN samples. Here, the ratio of the number of divacancy to SW defects is defined as the amorphous defect ratio of 2D-aBN. And in order to distinguish the defects concentration in the defective h-BN, the total defects concentration of amorphous h-BN is called the amorphous concentration.

First, we specified the defect ratio to be 1: 1, and studied the effect of amorphous concentration on the thermal conductivity of 2D-aBN at 300 K and 500 K respectively. A horizontal analysis of the results in Fig. 7 shows that the thermal conductivity of 2D-aBN has a cliff-like decline, which result in the thermal conductivity almost an order of magnitude smaller than that of the pristine h-BN. As the amorphous concentration increases, the thermal conductivity of the sample continues to decline and eventually tends to be stable. Then the vertical analysis of the results is carried out by a graph based on logarithmic coordinates. The thermal conductivity of the pristine h-BN is about 656 $Wm^{-1} K^{-1}$ and 176 $Wm^{-1} K^{-1}$ at 300 K and 500 K, respectively. The former is more than three times than the latter. However, with the increase of the amorphous concentration, the difference between the thermal conductivity of 2D-aBN at these two different temperature conditions is very slight. This means that the thermal conductivity of 2D-aBN is not sensitive to temperature. This is because in the pristine h-BN, phonon–phonon scattering plays a decisive role in thermal resistance. At relatively higher temperature, more intense atomic motion enhances phonon–phonon scattering, which leads to significant decrease in thermal conductivity. In the 2D-aBN, the dominance of phonon-defect scattering on thermal resistance weakens the effect of phonon–phonon scattering. It means that phonon–phonon scattering and phonon-defect scattering, the two determinants of thermal resistance, restrict and influence each other, which corresponds to the macro-determined effect of temperature and defects on the thermal conductivity of h-BN. In Fig. 7, the obtained total thermal conductivity was decomposed into two parts: in-plane and out-of-plane for comparative study, which corresponds to the respective contributions of different types of phonons to the thermal conductivity. It is not difficult to find that temperature has almost no effect on the ratio of in-plane and out-of-plane thermal conductivity. With the increase of the amorphous concentration, the out-of-plane part, which originally accounted for 60% of the overall thermal conductivity of pristine h-BN, was increasingly inhibited. The thermal conductivity of 2D-aBN whose amorphous concentration is higher than 20% is almost entirely derived from the contribution of the in-plane part. This is because the wide distribution of defects greatly affects the out-of-plane vibration mode of the structure, which is also a major factor influencing the weakening of thermal conductivity by the presence of defects.

In order to more clearly explain the fundamental mechanism of the influence of amorphization on the thermal conductivity of h-BN, the calculated DOS of the pristine h-BN and the above-mentioned 2D-aBN with amorphous concentration of 10% and 40% is compared. It can be seen from Fig. 8 that as the amorphous concentration increases, the peaks in the calculated DOS are attenuated and most of the peaks are broadened. This means that the lifetime of the phonon is weakened, which is proportional to the thermal conductivity. In addition, the reduction of DOS in the low frequency band, which is as the main thermal carrier, is also in good agreement with the results in Fig. 7. The out-of-plane mean-square-displacement (MSD) of 2D-aBN at the above four different amorphous concentrations under the two temperature conditions of 300 K and 500 K were also studied. The out-of-plane MSD of 2D materials can intuitively reflect the off-plane vibration state of atoms, which can well reflect the influence of amorphous concentration on the out-of-plane vibration of 2D-aBN atoms. The out-of-plane MSD of 2D-aBN is calculated by the following formula:

$$MSD(t) = \langle \frac{1}{N} \cdot \sum_{i=1}^{N} |z_i(t + t_0) - z_i(t_0)|^2 \rangle \quad (8)$$

where N is the number of atoms, $z_i(t)$ represents the z coordinate of the atom with the sequence number of $i$at time t. And $\langle\rangle$ is the ensemble average, which is replaced by the average of the time origin $t_0$in the MD simulation. As shown in Fig. 9, with the increase of the amorphous concentration, the out-of-plane MSD of the atoms at each temperature both showed an upward trend. This is because the existence of defects

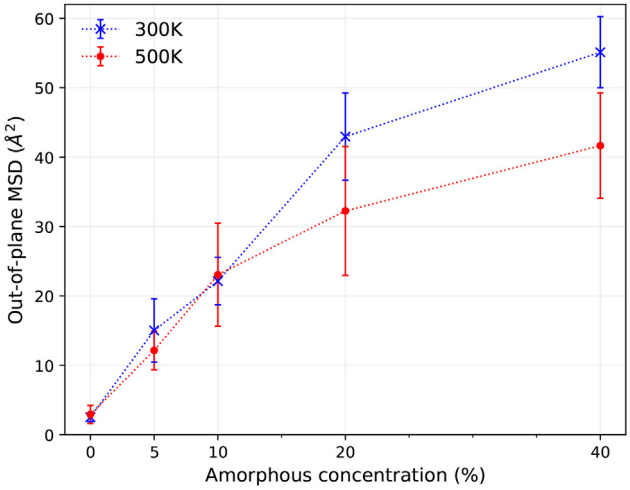

Fig. 9. The relationship between the out-of-plane mean square displacement (MSD) of 2D-aBN and the amorphous concentration at the temperature of 300 K and 500 K (The error value were calculated from the standard deviation of twenty independent simulation results).

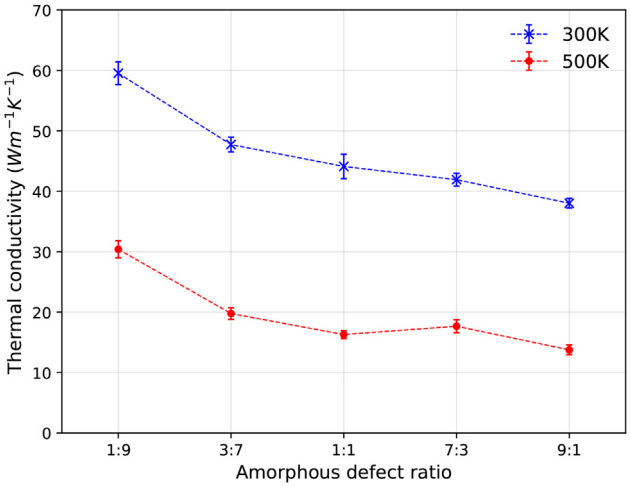

Fig. 10. The relationship between the thermal conductivity of 2D-aBN with an amorphous concentration of 10% and the amorphous defect ratio at a temperature of 300 K and 500 K; As mentioned above, the amorphous defect ratio is defined as the ratio of the number of divacancy defects to the number of the SW defects.

loses some of the constraints between the atoms and intensifies the out-of-plane vibrations of them. In the region where the amorphous concentration is less than 20%, the effect of temperature on the out-of-plane MSD is relatively small. However, in other parts, the MSD of the 2D-aBN atom out-of-plane at 300 K is significantly greater than 500 K. At higher temperatures, atoms have more violent vibrations, which is also reflected in the 500 K case of out-of-plane MSD calculation results generally with a wider error range.

In addition, the effect of the amorphous defect ratio of 2D-aBN on its thermal conductivity was also discussed. The 2D-aBN with an amorphous concentration of 10% was selected as the sample. At two temperatures of 300 K and 500 K, the thermal conductivity of the samples at five different amorphous defect ratios were compared. As presented in Fig. 10, at a certain amorphous concentration, the thermal conductivity of 2D-aBN is negatively correlated with the proportion of double vacancy defects in amorphous defects. And this relationship seems not to be affected by temperature. It is in good agreement with the previous findings, that under the same conditions, the divacancy defects has a weaker effect on the thermal conductivity of h-BN than the SW defects. The above findings mean that the thermal conductivity of 2D-aBN can be adjusted by adjusting the amorphous defect ratio, which is of great significance for h-BN defect engineering. In some specific application scenarios, the amorphous defect ratio can be used as an effective auxiliary control method for 2D-aBN thermal conductivity in addition to the adjustment of amorphous concentration. And on this basis, it can take into account the other physical and chemical properties of the two defects to optimize the structure.

4. Conclusion

In summary, we conducted extensive studies on the thermal transport properties of the monolayer h-BN transition from the defect state to the amorphous state based on the efficient HNEMD method. In the defect state h-BN, we found that three kinds of defects widely existing in 2D materials, including monovacancy, divacancy and SW defects, have a significant weakening effect on thermal conductivity of h-BN. The monovacancy and divacancy defects of the same concentration show almost the same weakening ability, and were significantly greater than the effect of SW defects on the thermal conductivity of h-BN. With the increase of the defect concentration, the thermal conductivity of the three kinds of defective h-BN has experienced a cliff-like decline in the low concentration stage and a relatively steady state in the high concentration stage. Then we introduced numerous divacancy and SW defects into the pristine h-BN to realize the transition from the defect state to the amorphous state of h-BN. By studying the thermal conductivity of 2D-aBN with different amorphous concentrations at 300 K and 500 K, it is found that while having a low thermal conductivity, the thermal conductivity of 2D-aBN is not sensitive to temperature. In addition, in 2D-aBN, both the amorphous concentration and the amorphous defect ratio have an obvious and regular effect on their thermal conductivity, which provides more specific possibilities for its regulation. For the above results, we also explained the change of h-BN thermal transport properties from the phonon perspective through the calculated DOS, and discussed the root cause of the corresponding thermal conductivity change. These findings have possible extension to the application of h-BN defect engineering in thermal management and thermal design of nanomaterials.

CRediT authorship contribution statement

Xin Wu: Conceptualization, Methodology, Software, Validation, Formal analysis, Investigation, Writing - original draft, Writing - review & editing, Visualization. **Qiang Han:** Resources, Supervision, Project administration, Funding acquisition.

Declaration of Competing Interest

The authors declare that they have no known competing financial interests or personal relationships that could have appeared to influence the work reported in this paper.

Acknowledgments

The authors are grateful for support from the National Natural Science Foundation of China (11972160), Guangdong Basic and Applied Basic Research Foundation (2019A1515011900), Science and Technology Program of Guangzhou, China (202002030367).

References

[1] H. Yi, M. Yan, D. Huang, G. Zeng, C. Lai, M. Li, X. Huo, L. Qin, S. Liu, X. Liu, B. Li, H. Wang, M. Shen, Y. Fu, X. Guo, Synergistic effect of artificial enzyme and 2d nanostructured bi2wo6 for eco-friendly and efficient biomimetic photocatalysis, Appl. Catal., B 250 (2019) 52–62, https://doi.org/10.1016/j.apcatb.2019.03.008.
[2] Y. Cao, V. Fatemi, S. Fang, K. Watanabe, T. Taniguchi, E. Kaxiras, P. Jarillo-Herrero,

Unconventional superconductivity in magic-angle graphene superlattices, Nature 556 (2018) 43–50, https://doi.org/10.1038/nature26160.
[3] K. Watanabe, T. Taniguchi, H. Kanda, Direct-bandgap properties and evidence for ultraviolet lasing of hexagonal boron nitride single crystal, ACS Nano 3 (2004) 404–409, https://doi.org/10.1038/nmat1134.
[4] T.T. Tran, C. Elbadawi, D. Totonjian, C.J. Lobo, G. Grosso, H. Moon, D.R. Englund, M.J. Ford, I. Aharonovich, M. Toth, Robust multicolor single photon emission from point defects in hexagonal boron nitride, ACS Nano 10 (2016) 7331–7338, https://doi.org/10.1021/acsnano.6b03602.
[5] L. Song, L. Ci, H. Lu, P.B. Sorokin, C. Jin, J. Ni, A.G. Kvashnin, D.G. Kvashnin, J. Lou, I. Yakobsonb, P.M. Ajayan, Large scale growth and characterization of atomic hexagonal boron nitride layers, Nano Lett. 10 (2010) 3209–3215, https://doi.org/10.1021/nl1022139.
[6] Q. Peng, W. Ji, S. De, Mechanical properties of the hexagonal boron nitride monolayer: ab initio study, Comp. Mater. Sci. 56 (2012) 11–17, https://doi.org/10.1016/j.commatsci.2011.12.029.
[7] E.K. Sichel, R.E. Miller, M.S. Abrahams, C.J. Buiocchi, Heat capacity and thermal conductivity of hexagonal pyrolytic boron nitride, Phys. Rev. B 13 (1976) 4607–4611, https://doi.org/10.1103/PhysRevB.13.4607.
[8] I. Jo, M.T. Pettes, J. Kim, K. Watanabe, T. Taniguchi, Z. Yao, L. Shi, Thermal conductivity and phonon transport in suspended few-layer hexagonal boron nitride, Nano Lett. 13 (2013) 550–554, https://doi.org/10.1021/nl304060g.
[9] C. Wang, J. Guo, L. Dong, A. Aiyiti, X. Xu, B. Li, Superior thermal conductivity in suspended bilayer hexagonal boron nitride, Sci. Rep. 6 (2016) 25334, https://doi.org/10.1038/srep25334.
[10] H. Ying, A. Moore, J. Cui, Y. Liu, D. Li, S. Han, Y. Yao, Z. Wang, L. Wang, S. Chen, Tailoring the thermal transport properties of monolayer hexagonal boron nitride by grain size engineering, 2D, Mater 7 (2019) 015031, https://doi.org/10.1088/2053-1583/ab5ae0.
[11] I.C. Taskin, O. Sen, M. Emanet, M. Culha, B. Yilmaz, Hexagonal boron nitrides reduce the oxidative stress on cells, Nanotechnology 31 (2020), https://doi.org/10.1088/1361-6528/ab6fdc 215101.
[12] L. Shen, Y. Zhao, Y. Wang, R. Song, Q. Yao, S. Chen, Y. Chai, A long-term corrosion barrier with an insulating boron nitride monolayer, J. Mater. Chem. A 4 (2016) 5044–5050, https://doi.org/10.1039/c6ta01604a.
[13] L. Wang, B. Wu, J. Chen, H. Liu, P. Hu, Y. Liu, Monolayer hexagonal boron nitride films with large domain size and clean interface for enhancing the mobility of graphene-based field-effect transistors, Adv. Mater. 26 (2014) 1559–1564, https://doi.org/10.1002/adma.201304937.
[14] Y. Wang, L. Xu, Z. Yang, H. Xie, P. Jiang, J. Dai, W. Luo, Y. Yao, E. Hitz, R. Yang, B. Yang, L. Hu, High temperature thermal management with boron nitride nanosheets, Nanoscale 10 (2017) 167–173, https://doi.org/10.1039/c7nr07058f.
[15] L. Lindsay, D.A. Broido, Enhanced thermal conductivity and isotope effect in single-layer hexagonal boron nitride, Phys. Rev. B 84 (2011), https://doi.org/10.1103/PhysRevB.84.155421 155421.
[16] D. Pacilé, J.C. Meyer, Ç.Ö. Girit, A. Zettl, The two-dimensional phase of boron nitride: Few-atomic-layer sheets and suspended membranes, Nano Today 92 (2004), https://doi.org/10.1063/1.2903702 133107.
[17] T.A. Chen, C.P. Chuu, C.C. Tseng, C.K. Wen, H.P. Wong, S. Pan, R. Li, T.A. Chao, W.C. Chueh, Y. Zhang, Q. Fu, B.I. Yakobson, W.H. Chang, L.J. Li, Wafer-scale single-crystal hexagonal boron nitride monolayers on cu (111), Nature 579 (2020) 219–223, https://doi.org/10.1038/s41586-020-2009-2.
[18] W. Wegner, K.J. Fijalkowski, W. Grochala, A low temperature pyrolytic route to amorphous quasi-hexagonal boron nitride from hydrogen rich (nh4)3mg(bh4)5, Dalton Trans. 49 (2020) 336–342, https://doi.org/10.1039/c9dt03766g.
[19] Y.Y. Liu, X.L. Zou, I.Y. Boris, Dislocations and grain boundaries in two-dimensional boron nitride, ACS Nano 6 (2012) 7053–7058, https://doi.org/10.1021/nn302099q.
[20] A.L. Gibb, N. Alem, J.H. Chen, K.J. Erickson, J. Ciston, A. Gautam, M. Linck, A. Zettl, Atomic resolution imaging of grain boundary defects in monolayer chemical vapor deposition-grown hexagonal boron nitride, J. Am. Chem. Soc. 135 (2013) 6758–6761, https://doi.org/10.1021/ja400637n.
[21] P.K. Schelling, S.R. Phillpot, P. Keblinski, Comparison of atomic-level simulation methods for computing thermal conductivity, Phys. Rev. B 65 (2002), https://doi.org/10.1103/PhysRevB.65.144306 144306.
[22] Z. Fan, L.F.C. Pereira, P. Hirvonen, M.M. Ervasti, K.R. Elder, D. Donadio, T. Ala-Nissila, A. Harju, Thermal conductivity decomposition in two-dimensional materials: application to graphene, Phys. Rev. B 95 (2017), https://doi.org/10.1103/PhysRevB.95.144309 144309.
[23] S. Plimpton, Fast parallel algorithms for short-range molecular dynamics, J. Comput. Phys. 117 (1993) 1–19, https://doi.org/10.2172/10176421.
[24] Y.C. Chen, S.C. Lee, T.H. Liu, C.C. Chang, Thermal conductivity of boron nitride nanoribbons: anisotropic effects and boundary scattering, Int. J. Therm. Sci. 94 (2015) 72–78, https://doi.org/10.1016/j.ijthermalsci.2015.02.005.
[25] T. Zhu, E. Ertekin, Resolving anomalous strain effects on two-dimensional phonon flows: the cases of graphene, boron nitride, and planar superlattices, Phys. Rev. B 91 (2015), https://doi.org/10.1103/PhysRevB.91.205429 205429.
[26] S.J. Mahdizadeh, E.K. Goharshadi, G. Akhlamadi, Thermo-mechanical properties of boron nitride nanoribbons: a molecular dynamics simulation study, J. Mol. Graph. Model 68 (2016) 11–13, https://doi.org/10.1016/j.jmgm.2016.05.008.
[27] A.I. Khan, I.A. Navid, M. Noshin, S. Subrina, Thermal transport characterization of hexagonal boron nitride nanoribbons using molecular dynamics simulation, AIP Adv. 44 (2017), https://doi.org/10.1063/1.4997036 105110.
[28] B. Mortazavi, Y. Rémond, Investigation of tensile response and thermal conductivity of boron-nitride nanosheets using molecular dynamics simulations, Physica E 44 (2012) 1846–1852, https://doi.org/10.1016/j.physe.2012.05.007.
[29] B. Mortazavi, L.F.C. Pereira, J.W. Jiang, T. Rabczuk, Modelling heat conduction in polycrystalline hexagonal boron-nitride films, Sci. Rep. 5 (2015) 13228, https://doi.org/10.1038/srep13228.
[30] Z. Fan, L.F.C. Pereira, Hui-Qiong Wang, J.-C. Zheng, D. Donadio, A. Harju, Force and heat current formulas for many-body potentials in molecular dynamics simulations with applications to thermal conductivity calculations, Phys. Rev. B 92 (2015) 094301, https://doi.org/10.1103/PhysRevB.92.094301.
[31] P. Boone, H. Babaei, C.E. Wilmer, Heat flux for many-body interactions: corrections to lammps, J. Chem. Theory Comput. 15 (2019) 5579–5587, https://doi.org/10.1021/acs.jctc.9b00252.
[32] D.J. Evans, Homogeneous nemd algorithm for thermal conductivity application of non-canonical linear response theory, Phys. Lett. A 91 (1982) 457–460, https://doi.org/10.1016/0375-9601(82)90748-4.
[33] K.K. Mandadapu, R.E. Jones, P. Papadopoulos, A homogeneous nonequilibrium molecular dynamics method for calculating thermal conductivity with a three-body potential, J. Chem. Phys. 130 (2009), https://doi.org/10.1063/1.3141982 204106.
[34] Zheyong Fan, H. Dong, A. Harju, T. Ala-Nissila, Homogeneous nonequilibrium molecular dynamics method for heat transport and spectral decomposition with many-body potentials, Phys. Rev. B 99 (2019) 064308, https://doi.org/10.1103/PhysRevB.99.064308.
[35] K. Xu, Z. Fan, J. Zhang, N. Wei, T. Ala-Nissila, Thermal transport properties of single-layer black phosphorus from extensive molecular dynamics simulations, Modell. Simul. Mater. Sci. Eng. 26 (2018), https://doi.org/10.1088/1361-651X/aae180 085001.
[36] H. Dong, P. Hirvonen, Z. Fan, T. Ala-Nissila, Heat transport in pristine and polycrystalline single-layer hexagonal boron nitride, Phys. Chem. Chem. Phys. 20 (2018) 24602–24612, https://doi.org/10.1039/c8cp05159c.
[37] Z. Fan, W. Chen, V. Vierimaa, A. Harju, Efficient molecular dynamics simulations with many-body potentials on graphics processing units, Comput. Phys. Commun. 218 (2017) 10–16, https://doi.org/10.1016/j.cpc.2017.05.003.
[38] Z. Fan, T. Siro, A. Harju, Accelerated molecular dynamics force evaluation on graphics processing units for thermal conductivity calculations, Comput. Phys. Commun. 184 (2013) 1414–1425, https://doi.org/10.1016/j.cpc.2013.01.008.
[39] B. Mortazavi, Zheyong Fan, L.F.C. Pereira, A. Harju, T. Rabczuk, Amorphized graphene: a stiff material with low thermal conductivity, Carbon 103 (2016) 318–326, https://doi.org/10.1016/j.carbon.2016.03.007.
[40] C. Sevik, A. Kinaci, J.B. Haskins, T. Cagn, Characterization of thermal transport in low-dimensional boron nitride nanostructures, Phys. Rev. B 84 (2011), https://doi.org/10.1103/PhysRevB.84.085409 085409.
[41] N. Alem, R. Erni, C. Kisielowski, M.D. Rossell, W. Gannett, A. Zettl, Atomically thin hexagonal boron nitride probed by ultrahigh-resolution transmission electron microscopy, Phys. Rev. B 80 (2009), https://doi.org/10.1103/PhysRevB.80.155425 155425.
[42] Q. Li, X. Zou, M. Liu, J. Sun, Y. Gao, Y. Qi, X. Zhou, B.I. Yakobson, Y. Zhang, Z. Liu, Grain boundary structures and electronic properties of hexagonal boron nitride on cu(111), Nano Lett. 15 (2015) 5804–5810, https://doi.org/10.1021/acs.nanolett.5b01852.
[43] E.A. Almahmoud, J.A. Talla, H. Abu-Farsakh, Electronic properties of defective boron nitride mono-sheets under the influence of an external electric field, Semicond. Sci. Technol. 35 (2020), https://doi.org/10.1088/1361-6641/ab5ece 025014.
[44] J. Kotakoski, A.V. Krasheninnikov, U. Kaiser, J.C. Meyer, From point defects in graphene to two-dimensional amorphous carbon, Phys. Rev. Lett. 106 (2011), https://doi.org/10.1103/PhysRevLett.106.105505 105505.
[45] J. Kotakoski, C. Brand, Y. Lilach, O. Cheshnovsky, C. Mangler, M. Arndt, J.C. Meyer, Toward two-dimensional all-carbon heterostructures via ion beam patterning of single-layer graphene, Nano Lett. 15 (2015) 5944–5949, https://doi.org/10.1021/acs.nanolett.5b02063.
[46] C.T. Toh, H. Zhang, J. Lin, A.S. Mayorov, Y.P. Wang, C.M. Orofeo, D.B. Ferry, H. Andersen, N. Kakenov, Z. Guo, I.H. Abidi, H. Sims, K. Suenaga, S.T. Pantelides, B. Ozyilmaz, Synthesis and properties of free-standing monolayer amorphous carbon, Nature 557 (2020) 199–203, https://doi.org/10.1038/s41586-019-1871-2.
[47] A. Kinaci, J.B. Haskins, T. Cagin, On calculation of thermal conductivity from einstein relation in equilibrium molecular dynamics, J. Chem. Phys. 137 (2012), https://doi.org/10.1038/s41586-019-1871-2 014106.
[48] M.S. Green, Markoff random processes and the statistical mechanics of time-dependent phenomena. ii. irreversible processes in fluids, J. Chem. Phys. 22 (1954) 398–413, https://doi.org/10.1063/1.1740082.
[49] R. Kubo, Statistical-mechanical theory of irreversible processes. i. general theory and simple applications to magnetic and conduction problems, J. Phys. Soc. Jpn. 12 (1957) 570–586, https://doi.org/10.1143/JPSJ.12.570.
[50] J.E. Turney, E.S. Landry, A.J.H. McGaughey, C.H. Amon, Predicting phonon properties and thermal conductivity from anharmonic lattice dynamics calculations and molecular dynamics simulations, Phys. Rev. B 79 (2009), https://doi.org/10.1103/PhysRevB.79.064301 064301.